Article | Open Access

Energy Materials

Wardani *et al. Energy Mater.* **2026**, *6*, 600091 **DOI:**10.20517/energymater.2026.85

Bilateral coordination interfaces enable long-term stable organic solar cells under multiple stress conditions

Nurul Kusuma Wardani[1,2], Muhammad Jahandar[1], Yong Hyun Kim[2], Soyeon Kim[1,*], Dong Chan Lim[1,*]

Keywords:
Bilateral interface engineering, coordination-engineered cathode, self-assembled monolayer, operational stability

Citation: Wardani, N. K.; Jahandar, M.; Kim, Y. H.; Kim, S.; Lim, D. C. Bilateral coordination interfaces enable long-term stable organic solar cells under multiple stress conditions. *Energy Mater.* **2026**, *6*, 600091. https://dx.doi.org/10.20517/energymater.2026.85

Received: 24 Apr 2026
First Decision: 16 Jun 2026
Revised: 29 Jun 2026
Accepted: 27 Jul 2026
Published: 31 Jul 2026

Academic Editor: Federico Bella
Copy Editor: Fangling Lan
Production Editor: Fangling Lan

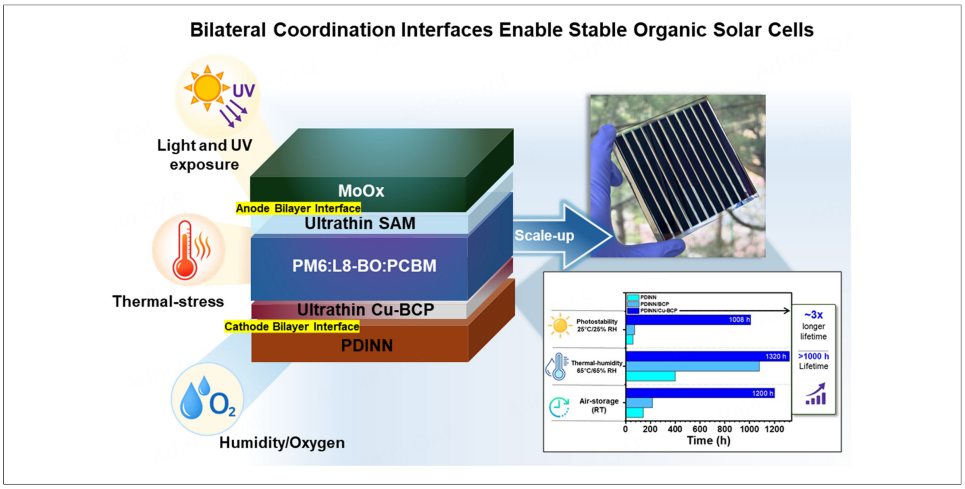

Abstract

Achieving long-term operational stability alongside high power conversion efficiency remains one of the most critical challenges for organic solar cells (OSCs), as interfacial degradation under heat, humidity, and continuous illumination severely limits device lifetime. Although many studies report improved stability under individual stress conditions, few OSC studies have demonstrated extended durability across multiple stress conditions. Here, we report a bilateral bilayer interface engineering strategy centered on a novel coordination-engineered cathode stabilization material, Cu-bathocuproine (BCP), formed by coordinating Cu with conventional BCP. Introduced as an overlayer on aliphatic amine-functionalized perylene-diimide (PDINN), Cu-BCP serves as an efficient electron-extraction interlayer and a chemically stabilized buffer that suppresses detrimental interfacial reactions with the non-fullerene acceptor. Combined with a self-assembled monolayer/metal oxide anode bilayer, [2-(9H-carbazol-9-yl)ethyl]phosphonic acid (2PACz)/MoO_x, OSCs with the structure of indium tin oxide (ITO)/PDINN/Cu-BCP/PM6:L8-BO:$PC_{71}BM$/2PACz/MoO_x/Ag achieve a power conversion efficiency of 16.70%, surpassing the reference devices based on PDINN (14.58%) and PDINN/BCP (15.05%). Importantly, the bilateral bilayer devices exhibit substantially enhanced

[1]Energy and Environment Materials Research Division, Korea Institute of Materials Science (KIMS), Changwon 51508, Republic of Korea.
[2]Department of Smart Green Technology Engineering, Pukyong National University, Busan 48513, Republic of Korea.

***Correspondence to:** Dr. Soyeon Kim, Dr. Dong Chan Lim, Energy and Environment Materials Research Division, Korea Institute of Materials Science (KIMS), Changwon 51508, Republic of Korea. E-mail: kimso1965@kims.re.kr; dclim@kims.re.kr

durability under multiple independent stress conditions, retaining 80% of their initial efficiency after 1,200 h in air storage, 1,320 h at 65 °C/65% relative humidity, and 1,008 h under continuous 1-sun illumination, corresponding to the longest T_{80} lifetime among PDINN-based devices. The improved stability is associated with suppressed trap-assisted recombination, reduced leakage current, and lower charge-transfer resistance. Moreover, large-area modules deliver an efficiency of 14.57% with a 54 cm^2 active area, indicating an 87% cell-to-module ratio. These results demonstrate that ultrathin stabilization-layer design within bilateral bilayer interfaces is an effective route toward efficient, stable, and scalable OSCs.

INTRODUCTION

In recent years, organic solar cells (OSCs) have been rapidly developed, exhibiting power conversion efficiencies (PCEs) that exceed 19%. This improvement is mainly due to the development of non-fullerene acceptors (NFAs), improved control over bulk-heterojunction (BHJ) morphology, and the emergence of self-assembled monolayer (SAM)-based hole-selective contacts[1-6]. Despite these remarkable gains in efficiency, long-term operational stability remains a major obstacle to practical deployment, particularly under realistic stress conditions involving heat, moisture, and continuous illumination[7-9]. Moreover, while many previous studies have achieved strong stability under one specific stress condition, and in some cases under three, it remains uncommon for a single OSC study to clearly demonstrate extended durability across all major independent stress modes relevant to practical operation[10-12]. Because interfacial degradation is often one of the earliest and most severe failure pathways in OSCs, developing robust interfacial materials is currently as important as improving the photoactive layer itself.

In inverted OSC architectures, the electron-collecting interface is especially critical because it governs both charge-selective extraction and interfacial chemical stability. ZnO has been widely used as an electron transport layer (ETL), yet its surface defects and photocatalytic activity are well known to accelerate interfacial degradation and compromise photostability[13-15]. These limitations have stimulated growing interest in alternative cathode interlayers (CILs) that can maintain efficient electron extraction while minimizing interfacial instability. Among them, water/alcohol-processable organic cathode interlayer materials (CIMs), such as poly[(9,9-bis(3′-((*N*,*N*-dimethyl)-*N*-ethylammonium)-propyl)-2,7-fluorene)-*alt*-2,7-(9,9-dioctylfluorene)] (PFN-Br), polyethyleneimineethoxylated (PEIE), and related amine-containing materials, offer several advantages, including effective defect passivation, low-temperature processing, and improved compatibility with NFA-based active layers[16-18]. In particular, aliphatic amine-functionalized perylene-diimide (PDINN) has emerged as a highly effective cathode interlayer, providing favorable energy-level alignment and enabling high initial efficiencies across a wide range of OSC systems[19-21]. However, PDINN primarily addresses electronic contact formation and does not inherently provide sufficient chemical protection against prolonged thermal, humid, or photo-induced interfacial degradation. As a result, the cathode-side interface remains vulnerable under extended operation.

A promising route to address this issue is to move beyond the conventional role of bilayer interfacial contacts. In most OSC bilayers, the additional layer is mainly introduced to tune the work function (WF), improve energy alignment, or facilitate charge extraction. Alternatively, an ultrathin constituent layer may be incorporated within the bilayer to specifically function as a stabilization layer. Such a design would enable the bilayer to combine electronic selectivity with chemical protection, thereby simultaneously addressing efficiency and durability concerns. In this context, bathocuproine (BCP) and related phenanthroline-derived molecules are attractive starting materials because they are established cathode-side buffer materials in optoelectronic devices and possess favorable electron-transporting and hole/exciton-blocking properties[22,23]. However, pristine BCP can interact unfavorably with NFA-based active layers, leading to interfacial instability[22]. This highlights the need for a new material design approach in which a conventional interlayer

is transformed into a more chemically robust functional component rather than simply using it in its original form[24]. In this context, metal-ligand coordination is particularly attractive because it can modulate the ligand electronic structure, reduce chemical reactivity, stabilize interfacial energetics, and promote denser molecular packing[25-27]. Previous studies have shown that coordination-based cathode modification can effectively improve cathode contact properties. For example, phenanthroline coordination on ZnO has been used to tune the work function of metal-oxide cathode buffer layers, while Ag/phenanthroline coordination has been reported to promote coordination-assisted n-doping and improve electron injection in organic electronics[28,29]. Nevertheless, these approaches mainly focus on work-function modulation, electron injection, or doping behavior, and comparatively fewer studies have targeted cathode-side chemical stabilization at the CIL/NFA-containing active-layer interface under multiple operational stress conditions. Based on this concept, Cu-coordinated BCP (Cu-BCP) is a coordination-engineered interfacial material derived from conventional BCP, designed to act as an ultrathin chemically stabilized overlayer for ETLs while preserving efficient electron extraction.

Anode-side interlayers are also critical for achieving efficient and stable inverted OSCs. Among various hole-selective interlayers, SAMs, particularly [2-(9H-carbazol-9-yl)ethyl]phosphonic acid (2PACz), have been shown to improve energy-level alignment, suppress interfacial recombination, and simplify device fabrication[30,31]. In this study, we develop a bilateral bilayer interface engineering strategy that combines a coordination-engineered cathode bilayer (PDINN/Cu-BCP) with a SAM/metal oxide anode bilayer (2PACz/MoO_x). In contrast to previous studies that mainly focused on either cathode-side or anode-side interlayers separately, the present study integrates both interfaces into a bilateral bilayer design. Importantly, the cathode bilayer is not designed merely as a conventional dual-interlayer contact; rather, one of its constituent layers is an ultrathin coordination-engineered stabilization sublayer. PDINN functions as the primary electron-selective contact, while the ultrathin Cu-BCP overlayer acts as a coordination-engineered stabilization layer. Through Cu-N coordination, Cu-BCP modifies the nitrogen electronic environment of BCP, reduces unfavorable cathode-side interfacial reactivity, and helps preserve efficient electron extraction during device operation. At the anode side, the 2PACz/MoO_x bilayer provides a controlled and stable hole-collecting contact. Through the simultaneous engineering of both charge-extraction interfaces, the resulting OSCs achieve a high PCE of 16.70% and show markedly improved operational stability under multiple independent stress conditions, retaining 80% of their initial efficiency after 1,200 h in air storage, 1,320 h at 65 °C/65% relative humidity (RH), and 1,008 h under continuous 1-sun illumination. Moreover, large-area modules deliver 14.57% efficiency over a 54 cm^2 active area with an 87% cell-to-module (CTM) ratio. To the best of our knowledge, no single previous OSC study has clearly established more than 1,000 h of durability under air/ambient storage, humidity-containing thermal aging, and continuous illumination. Taken together, these results identify Cu-BCP as a promising coordination-engineered stabilization material for CILs and demonstrate that ultrathin stabilization-layer design within bilateral bilayer interfaces is an effective strategy for simultaneously advancing the efficiency, stability, and scalability of OSCs.

EXPERIMENTAL

Materials

The donor polymers PBDBT-2F (also referred to as PM6) and the NFA (L8-BO) were purchased from 1-Materials. The fullerene acceptor $PC_{71}BM$ was supplied by Sigma-Aldrich. PDINN (1-Materials) and 2PACz (TCI), as well as copper(II) chloride ($CuCl_2$, Sigma-Aldrich) and BCP (Sigma-Aldrich), were purchased commercially.

Device fabrication

For the CIL preparation, PDINN was dissolved in methanol at a concentration of 1 mg/mL and stirred at 500 rpm for 3 h at room temperature (RT, 25 ± 2 °C). Separately, the stock solution of BCP was prepared by dissolving BCP in 2-propanol to a concentration of 0.5 mg/mL, then stirring at 40 °C for 3 h. In another vial,

$CuCl_2$ was dissolved in 2-propanol to a concentration of 0.5 mg/mL, then stirred at 40 °C for 3 h. Next, Cu-BCP was prepared using a $CuCl_2$:BCP ratio of 1:5 (v/v) and stirred at 40 °C for at least 10 h. For anode-side modification, a 0.36 mg/mL solution of 2PACz was prepared in ethanol and sonicated for approximately 30 min. The glass/indium tin oxide (ITO) electrode substrate was first ultrasonicated in acetone and isopropanol for 15 min in each solvent, then oven-dried at 100 °C for 30 min. Prior to interlayer deposition, the ITO substrates were subjected to UV-ozone treatment for 1,000 s. Next, PDINN was coated at 3,000 rpm for 30 s, resulting in a thickness of approximately 15 nm, and then subjected to thermal annealing for 5 min at 100 °C. The BCP overlayer was introduced onto the PDINN layer by spin-coating at 4,000 rpm for 30 s, yielding a thickness of approximately 10 nm. The $CuCl_2$ ratio of 1:5 refers to the volume ratio (v/v) of the $CuCl_2$ and BCP stock solutions, and the resulting Cu-BCP overlayer exhibited an approximate thickness of 10 nm after spin-coating at 4,000 rpm for 30 s. After depositing the CIL, the active layer solution was initially prepared by dissolving the donor polymer (PM6), NFA (L8-BO), and the fullerene acceptor ($PC_{71}BM$) (PM6:L8-BO:$PC_{71}BM$) as the third component at a ratio of 1:1.2:0.1, with a total concentration of 16.5 mg/mL in chloroform containing 5 μL of 1,8-diiodoctane (DIO) as an additive. The solution was stirred at 500 rpm for 3 h at 40 °C. Next, the optimized photoactive blend was spin-coated at 4,000 rpm for 30 s, yielding an optimum film thickness of 120 nm. The active layers were thermally annealed at 80 °C for 10 min. Next, 2PACz was introduced onto the active layer at a spin speed of 5,000 rpm for 40 s, and the resulting 2PACz-coated active-layer film was then annealed at 100 °C for 5 min. Finally, to complete the device fabrication, the device was inserted into a thermal evaporator to deposit MoO_x (10 nm) and Ag (100 nm) under a pressure of 1×10^{-6} Torr. The defined device area was 0.14 cm^2.

Measurement and characterization

The optical properties, including the transmittance and absorbance, were measured using an ultraviolet-visible (UV-Vis) spectrometer (Cary 5000, Varian, USA). The surface morphology was investigated using atomic force microscopy (AFM; Park NX10, Park Systems, Republic of Korea). Water contact angle measurements were performed using a contact angle analyzer (Phoenix-300, SEO, Republic of Korea) to evaluate surface wettability. The WFs of the CILs were determined from the onset of the secondary electron cutoff region using ultraviolet photoelectron spectroscopy (UPS; MultiLab 2000, Thermo Scientific, UK). Current density-voltage (J-V) characteristics were measured in ambient air using a source meter (Keithley 2400A) under calibrated AM 1.5G illumination at 100 mW/cm^2. The illumination intensity was calibrated using a standard Si photodiode detector equipped with a KG-5 filter (Oriel 91150V, Newport, USA). External quantum efficiency (EQE) spectra were collected over the wavelength range of 300-1,000 nm using an EQE measurement system (Oriel IQE-200, Newport Co., USA). Electrochemical impedance spectroscopy (EIS) was carried out using an electrochemical impedance analyzer (CompactStat, Ivium Technologies, Netherlands) over the frequency range of 1 kHz to 1 MHz under dark conditions, with the applied bias set close to the open-circuit voltage (V_{OC}) of each device. The time-resolved photoluminescence (TRPL) decay transients were recorded at 635 nm under pulsed excitation at 405 nm.

RESULTS AND DISCUSSION

To enhance interfacial stability and charge extraction in inverted-structure OSCs, a coordination-engineered CIL comprising PDINN/Cu-BCP was developed. Figure 1A presents the molecular structures of the active-layer components and the design concept of the coordination-engineered CIL. In this strategy, pristine BCP is converted into Cu-BCP through coordination with copper, forming a coordination-locked overlayer on PDINN. As illustrated in Figure 1A, BCP coordinates with copper species to form a Cu-N coordination complex, denoted as Cu-BCP, thereby generating a coordination-locked interlayer on top of PDINN. This coordination interaction effectively suppresses the reactivity of nitrogen lone pairs in pristine BCP and promotes the formation of a denser, chemically stabilized interfacial layer, in agreement with a previous study showing that strong coordination between air-stable metal species and chelating organic ligands drives

complex formation and facilitates electron donation[32]. The corresponding device architecture is shown in Figure 1B, which consists of ITO/PDINN/Cu-BCP/PM6:L8-BO:$PC_{71}BM$/2PACz/MoO_x/Ag. To enhance hole extraction and reduce interfacial recombination, the 2PACz layer was used as an ultra-thin hole-selective interlayer that was coated on top of the active layer before MoO_x. Previous research demonstrated that hybrid SAM/MoO_x contacts in inverted devices can increase interfacial stability, minimize unfavorable direct interactions between MoO_x and the bulk heterojunction, and facilitate charge transport[33,34]. Thermally evaporated MoO_x is sensitive to temperature and deteriorates with increasing annealing temperature, and it can also spontaneously diffuse into underlying organic layers, leading to performance degradation over time[35]. Supplementary Figure 1 shows that introducing 2PACz onto the PM6:L8-BO:$PC_{71}BM$ film results in negligible changes in the absorption profile, suggesting that the optical characteristics of the active layer are well preserved. No noticeable spectral shift was observed following the introduction of 2PACz, indicating that the intrinsic optical properties of the active layer were preserved. The interfacial electronic characteristics of the modified ITO electrodes were further evaluated using UPS. As shown in Figure 1C, the WF of the modified ITO electrode is determined from the onset of the secondary-electron cutoff region in the UPS spectra. The calculated WFs are listed in Supplementary Table 1. Originally, the WF of ITO/PDINN was 4.10 eV, which decreased to 4.04 eV for ITO/PDINN/BCP and 3.94 eV for ITO/PDINN/Cu-BCP because of the formation of a strong interfacial dipole originating from the amine groups of PDINN. The modification of the ITO/PDINN layer with BCP and Cu-BCP can be attributed to the resulting lower WF values of 4.04 and 3.94 eV, respectively. This additional tuning of the WFs is beneficial for forming a favorable energy alignment with the LUMO level of the L8-BO acceptor, thereby facilitating more efficient electron extraction and charge transport[36,37]. The energy-level alignment of the device components is illustrated in Figure 1D, confirming that the PDINN/Cu-BCP interlayer forms a suitable cascade energy structure for electron transport. To examine how the BCP and Cu-BCP overlayers influence charge transport through the CIL, conductivity measurements were carried out using the device configuration ITO/PDINN/(BCP or Cu-BCP)/Ag, as shown in the inset of Figure 1E. As shown in Figure 1E, the electrical conductivity of the ITO/interlayer/Ag stacks gradually increases from 1.18×10^{-6} S/m for the PDINN to 1.29×10^{-6} S/m for the PDINN/BCP system, and it further increases to 1.50×10^{-6} S/m for PDINN/Cu-BCP (the conductivity values are summarized in Supplementary Table 2). In addition, the optical transmittance spectra of the modified electrodes [Figure 1F] indicate that the insertion of PDINN, BCP, or Cu-BCP layers has a negligible influence on the optical transparency of the electrode in the visible region.

The chemical compatibility between the L8-BO acceptor and the interlayer components was first examined using the absorption spectra to clarify the role of Cu-BCP in suppressing interfacial degradation. As shown in Figure 2A, mixing PDINN with L8-BO leads to a clear spectral perturbation in the visible region together with a visible color change, indicating a relatively strong chemical/electronic interaction between the acceptor and PDINN. This trend aligns with a previous study demonstrating that a CIL with amines can chemically react with NFAs, altering their original electronic structure[24]. While PDINN is a known efficient dipolar CIL, its amine-containing side chains can also create strong interfacial interactions with the active layer, which is beneficial electronically yet can become chemically problematic for reactive NFA systems[38]. By contrast, the spectra of L8-BO (dissolved in chloroform) mixed with BCP or Cu-BCP remain much closer to the spectrum of pristine L8-BO, suggesting that the BCP-based upper layer effectively mitigates direct perturbation of the acceptor. Conversely, phenanthroline-based interlayers with lower interfacial reactivity can prevent these chemical interactions at the cathode and thereby stabilize the system[39]. X-ray photoelectron spectroscopy (XPS) was conducted to understand the formation of the coordination-engineered Cu-containing cathode layer and the interfacial interactions between PDINN. The corresponding full survey spectra are provided in Supplementary Figure 2. As shown in Supplementary Figure 3, the C 1s spectra show that, after deposition of PDINN, PDINN/BCP, and PDINN/Cu-BCP, a pronounced C peak appears in the typical aromatic/adventitious carbon region (284.5-284.8 eV). This confirms successful

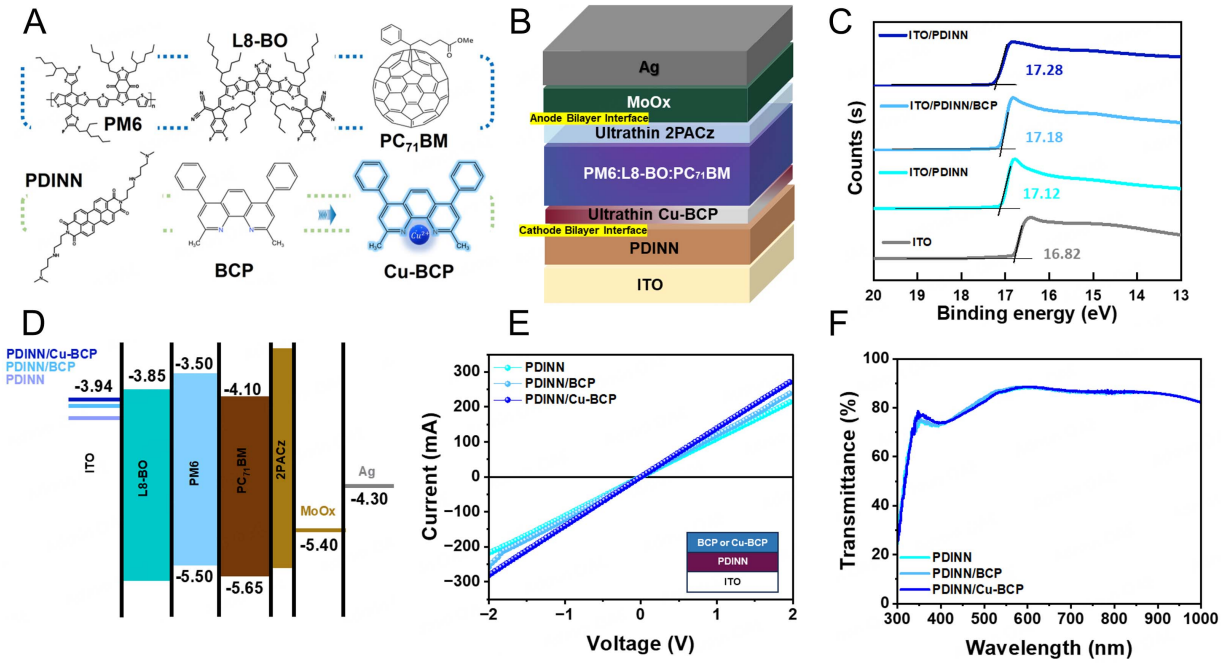

Figure 1. (A) Chemical structures of the photoactive materials (PM6:L8-BO:$PC_{71}BM$) and cathode interlayers components (PDINN, BCP and Cu-BCP); (B) inverted OSC device structure incorporating PDINN/Cu-BCP as bilayer ETLs and ultrathin 2PACz/MoO_x as a bilayer HTL; (C) UPS spectra of ITO, ITO/PDINN, ITO/PDINN/BCP, and ITO/PDINN/Cu-BCP; (D) energy level alignment of the inverted OSC device structure; (E) I-V characteristics of the ITO/PDINN-based interfacial stacks with BCP or Cu-BCP; (F) optical transmittance spectra of ITO substrates modified with PDINN, PDINN/BCP, and PDINN/Cu-BCP interlayers.

coverage of the ITO surface by the organic interlayers. More importantly, the In 3d doublet in Supplementary Figure 4 shows subtle but reproducible displacement after interlayer deposition, indicating that the electronic environment of the ITO surface is modified by PDINN and is further perturbed by the BCP-containing overlayers. Similar core-level shifts in modified ITO electrodes have been associated with interfacial dipole formation and WF/electrostatic redistribution, rather than necessarily with the formation of a new bulk indium compound. The N 1s spectra of the interlayer-only films provide direct evidence for systematic modification of the nitrogen electronic environment upon introducing BCP and Cu-BCP [Figure 2B]. Relative to PDINN alone, the N 1s signal of PDINN/BCP shifts to a slightly higher binding energy, reflecting a modified nitrogen chemical environment upon the introduction of the BCP overlayer. The O 1s spectra in Figure 2C further indicate that the deposition of PDINN, PDINN/BCP, and PDINN/Cu-BCP modifies the oxygen-containing surface environment of ITO. Although the O 1s region can include contributions from lattice oxygen, surface hydroxyl species, and adsorbed oxygen-containing species, the absence of new substrate-related features suggests that the observed changes are more reasonably attributed to surface coverage, passivation, and interfacial electronic redistribution rather than the destructive chemical transformation of ITO. Upon the incorporation of Cu-BCP, the N 1s peak shifts further to higher binding energy, as previously mentioned, which is consistent with electron-density withdrawal from nitrogen atoms upon Cu-N coordination. In this context, the N atoms become more electronically engaged, and their lone-pair availability is reduced, supporting the formation of a coordination-locked Cu-containing interlayer. The main XPS core-level peak positions are summarized in Supplementary Table 3 to facilitate comparison of the chemical shifts induced by BCP and Cu-BCP modification. This interpretation is further strengthened by the Cu 2p spectra as shown in Figure 2D, where the Cu $2p_{3/2}$ and Cu $2p_{1/2}$ features are clearly observed only for PDINN/Cu-BCP, directly confirming the successful incorporation of Cu-containing species into the BCP-based overlayer. Taken together, the C 1s, O 1s, In 3d, N 1s, and Cu 2p results indicate that Cu-BCP forms a chemically stabilized coordination-engineered overlayer on PDINN while preserving the integrity of the

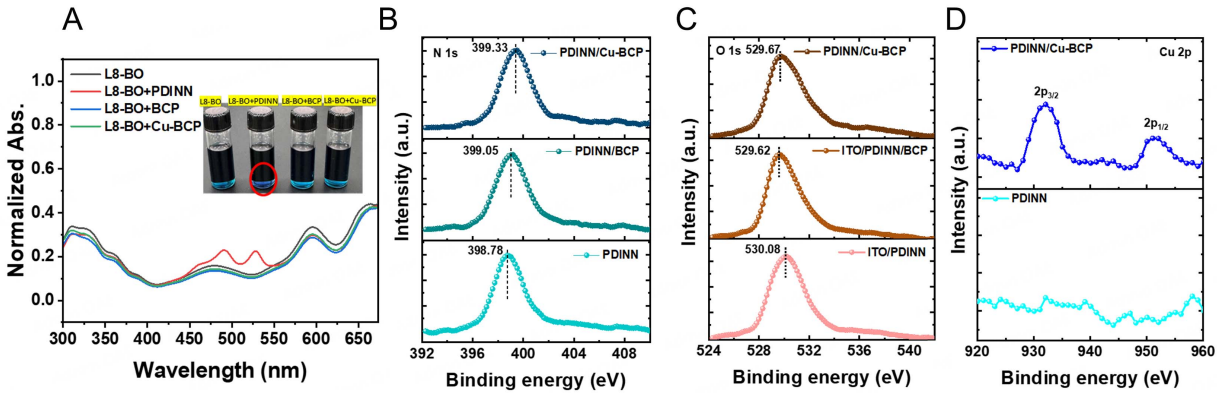

Figure 2. Optical and chemical interaction analysis of PDINN-based CILs. (A) Normalized UV-vis absorption profiles for neat L8-BO solution and L8-BO blended with PDINN, BCP, or Cu-BCP, with a photograph of the corresponding solution shown in the inset. XPS spectra of (B) N 1s element; (C) O 1s element of PDINN, PDINN/BCP, PDINN/Cu-BCP; and (D) Cu 2p element of PDINN *vs.* PDINN/Cu-BCP.

underlying electrode. To probe how the underlying interlayer influences the cathode-facing BHJ environment, N 1s spectra were measured after BHJ deposition [Supplementary Figure 5]. Notably, the detected N 1s signal in these BHJ-coated samples primarily originates from the nitrogen-containing acceptor (L8-BO) near the surface, with contributions from the buried interlayer attenuated by the overlying active layer. Therefore, the progressive shift from 398.61 eV (PDINN/BHJ) to 398.82 eV (PDINN/Cu-BCP/BHJ) reflects how the underlying Cu-coordinated interlayer modifies the local electrostatic and chemical environment experienced by the N-containing acceptor-rich region, rather than direct evidence of Cu-N bonding within the completed device stack. This interpretation is consistent with reports that phenanthroline-based CILs can strongly influence NFA-side interfacial chemistry and stability[40].

The morphology and wettability of the modified substrates were systematically examined because the surface characteristics of CIL-modified ITO can affect interfacial adhesion and electron-collection behavior. AFM analysis was performed to assess the morphological changes induced by the BCP overlayer and Cu-BCP coordination layer before and after coating the photoactive blend. As shown in Supplementary Figure 6, PDINN/BCP displays a slightly increased roughness (R_q = 1.115 nm) compared to PDINN, whereas PDINN/Cu-BCP exhibits marginally lower roughness (R_q = 0.962 nm). While these differences are modest, the consistently lower roughness of PDINN/Cu-BCP across both bare interlayer and BHJ-coated films suggests improved interfacial uniformity, which may contribute to reduced contact resistance and more stable device operation, as supported by the lower charge-transfer resistance and improved stability observed in the corresponding devices[41]. After photoactive layer coating, all films remain smooth, with R_q values of 1.584, 1.644, and 1.582 nm for PDINN, PDINN/BCP, and PDINN/Cu-BCP, respectively, indicating that none of the interlayers induces severe topographic instability during BHJ coating. Because the interfacial layers in OSCs are known to affect film morphology and recombination, as well as interfacial energetics, these AFM results indicate that Cu-BCP provides a more physically uniform cathode-side contact than BCP alone[41,42]. Water contact-angle measurements [Supplementary Figure 7] further reveal the systematic tuning of the surface wettability for various CILs, increasing from 41.4° for PDINN to 53.7° for PDINN/BCP and 57.9° for PDINN/Cu-BCP. The increased contact angle of PDINN/Cu-BCP indicates moderate surface polarity compared to PDINN. This change in wettability may influence BHJ deposition dynamics and interfacial contact quality. Combined with the AFM results showing uniform film formation, these data suggest that Cu-BCP provides balanced interfacial compatibility with the active layer, consistent with its beneficial effects on charge extraction and device stability. In particular, previous studies have shown that adjusting the surface free energy of interfacial layers can alter donor/acceptor distribution and active-layer morphology, while PDINN-type polar interlayers must balance the WF reduction against the risk of overly

high surface energy and inadequate physical contact with the active layer[21,43,44]. Therefore, the higher contact angle of PDINN/Cu-BCP suggests that Cu incorporation moderates the strong polarity of the PDINN-based cathode surface and provides a more balanced interface for PM6:L8-BO:$PC_{71}BM$ deposition. Based on this interfacial modification, the $CuCl_2$ mixing ratio was first optimized by comparing different volume ratios, including 1:0.5, 1:3, 1:5, and 1:7, using MoO_x alone as the HTL. Supplementary Table 4 summarizes the photovoltaic parameters obtained under different interlayer volume-ratio conditions. Among these devices, the 1:5 (v/v) ratio yielded the highest PCE of 15.24%, primarily due to improved V_{OC} and fill factor (FF) values. Therefore, the 1:5 (v/v) $CuCl_2$ ratio was selected as the optimized condition because it provides the best balance between Cu-N coordination-induced stabilization and efficient charge extraction. Using this optimized Cu-BCP condition, the intrinsic role of cathode-side bilayer engineering was then examined by comparing devices employing PDINN, PDINN/BCP, and PDINN/Cu-BCP CILs, as summarized in Supplementary Table 5. Starting from the PDINN single-layer cathode, the introduction of BCP improves the PCE from 13.69% to 14.62%, while further modification with Cu-BCP increases the PCE to 15.30%. This improvement is mainly driven by the enhancement in FF from 69% for PDINN to 71% for PDINN/BCP and 73% for PDINN/Cu-BCP, together with a moderate increase in V_{OC} from 0.82 to 0.84 and 0.85 V, respectively. By contrast, J_{SC} showed only a marginal variation, increasing from 24.19 mA cm^{-2} for PDINN to 24.51 and 24.53 mA cm^{-2} for PDINN/BCP and PDINN/Cu-BCP, respectively. These trends indicate that the cathode-side bilayer primarily improves charge extraction and reduces interfacial recombination/resistance losses, rather than significantly changing photocurrent generation.

Although the PDINN/Cu-BCP-based devices exhibited improved initial performance, the operational stability of these devices remains limited, as shown in Supplementary Figure 8. This suggests that cathode-side stabilization alone is insufficient to fully suppress device degradation, and that additional degradation pathways remain at the anode-side active-layer/MoO_x interface. Therefore, an ultrathin 2PACz interlayer was introduced before MoO_x to improve the active-layer/MoO_x interface, reduce unfavorable direct contact between the BHJ and MoO_x, and enhance hole extraction. As a result, the final bilateral bilayer interface design consists of PDINN/Cu-BCP as the cathode bilayer for electron extraction and cathode-side stabilization, and 2PACz/MoO_x as the anode bilayer for hole extraction and anode-side interfacial stabilization. For reference, the optimized organic CIL of PDINN was also compared with the conventional ZnO-based ETL. As shown in Supplementary Figure 9, the ZnO- and PDINN-based devices exhibit comparable initial photovoltaic performance under the 2PACz/MoO_x anode condition. However, under continuous 1-sun illumination, the ZnO-based device degrades much more rapidly than the PDINN-based device [Supplementary Figure 10]. The rapid decline in performance suggests serious deterioration of the cathode-side interface in the ZnO device. This poor durability is likely associated with the known susceptibility of ZnO to surface-defect-induced instability and photocatalytic-driven interfacial degradation, which can accelerate decomposition at the ZnO/active-layer interface. Therefore, despite its comparable initial efficiency, PDINN was selected as the more reliable organic CIL for further interfacial engineering. After establishing the intrinsic contribution of the cathode bilayer, an ultrathin 2PACz interlayer was introduced to improve the stability of the active layer/MoO_x interface, yielding a bilateral bilayer interface design composed of PDINN/Cu-BCP as the cathode bilayer and 2PACz/MoO_x as the anode bilayer. The corresponding comparison of photovoltaic parameters for devices with MoO_x and 2PACz/MoO_x is shown in Supplementary Figure 11, which clearly demonstrates that the highest performance is achieved when both bilayers are simultaneously integrated. Based on this PDINN result, additional modifications to BCP and Cu-BCP were subsequently explored to further optimize the cathode-layer interface and enhance stability, as explained later. The J-V characteristics in Figure 3A reveal improved device performance upon modifying PDINN with BCP and, more significantly, with Cu-BCP, with the addition of 2PACz as an HTL modification. The device parameters are listed in Table 1, and the PCE histogram is shown in Figure 3B. The reference device based on PDINN delivered a PCE of 14.58%, while further introducing BCP onto the

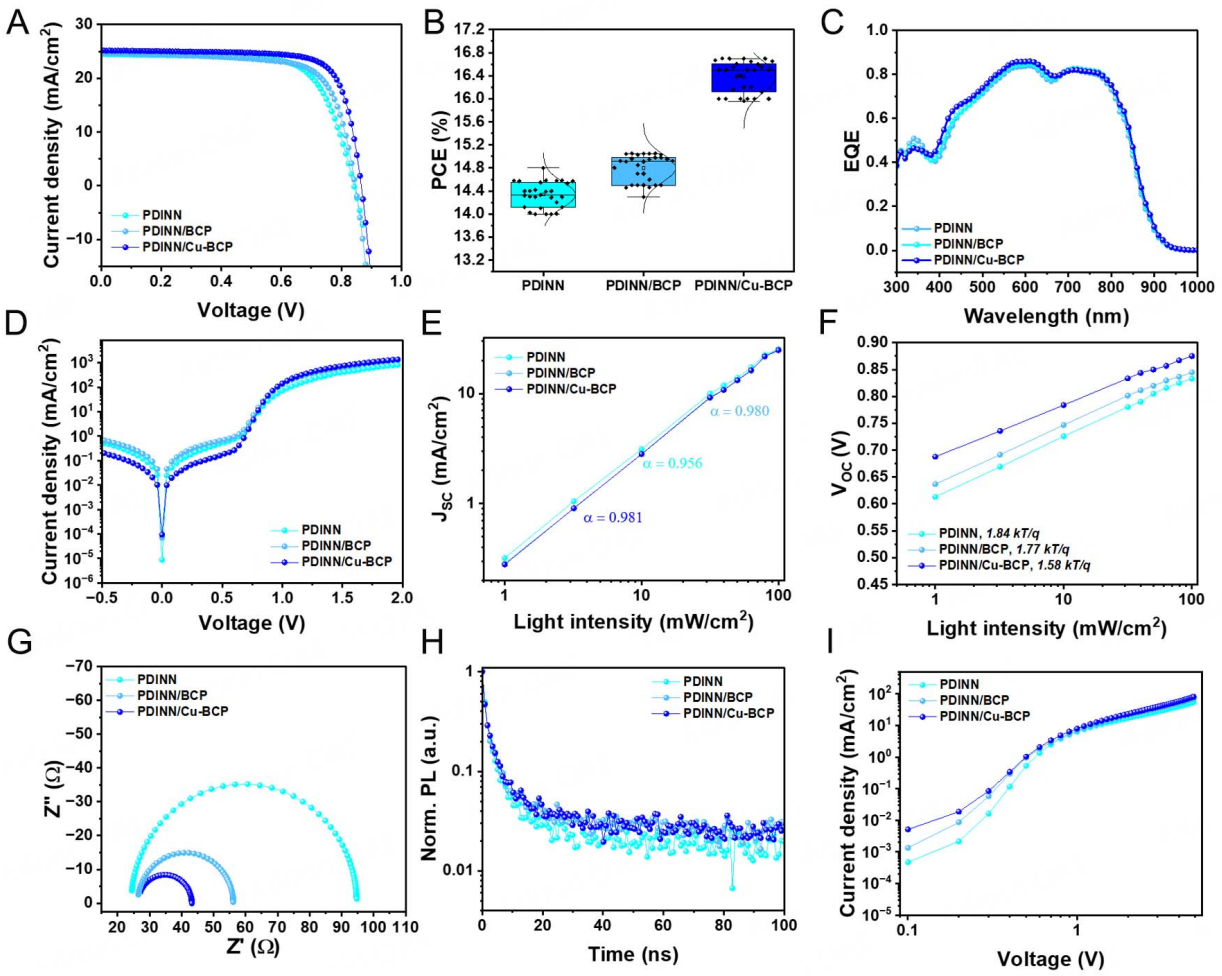

Figure 3. Device performance and interfacial charge-transport analysis of optimized ternary PM6:L8-BO:$PC_{71}BM$ OSCs with different cathode interlayers. (A) Current density-voltage (J-V) curves; (B) PCE statistics; (C) external quantum efficiency (EQE); (D) dark J-V characteristics; (E) J_{SC} and (F) V_{OC} as functions of the light intensity; (G) EIS spectra; (H) time-resolved photoluminescence (TRPL) decay curves; (I) space-charge-limited current (SCLC) characteristics.

PDINN layer slightly improved device performance, yielding a PCE of 15.05%. By contrast, the PDINN/Cu-BCP-based device exhibited the best performance, achieving a PCE of 16.70% with improved V_{OC} and FF values, while the change in J_{SC} was relatively small. These results indicate that incorporating Cu-BCP is highly effective at enhancing charge extraction and suppressing recombination losses at the cathode interface. The EQE was measured to obtain information on the photo-response of the OSC devices, as shown in Figure 3C. The integrated photocurrent density was 24.40 mA/cm², which is consistent with the J-V results. The PDINN/Cu-BCP-based device exhibits a slightly enhanced photoresponse across a broad wavelength range compared with the PDINN and PDINN/BCP devices, thereby accounting for its increased $J_{SC.}$ As shown in Figure 3D, the dark J-V characteristics were recorded in a voltage range of -0.5 to 2.0 V. In addition, the shunt resistance (R_{SH}) is closely related to leakage-current suppression. In the reverse-bias region from -0.5 to 0 V, the PDINN/Cu-BCP-based device exhibited a markedly lower leakage current than the PDINN- and PDINN/BCP-based devices, indicating improved blocking behavior and reduced interfacial leakage pathways. Under a forward bias above 1 V, the injection current of the PDINN/Cu-BCP bilayer device increased more prominently, suggesting more favorable charge injection/transport characteristics. To further investigate the recombination behavior, the light-intensity dependences of J_{SC} and V_{OC} were analyzed. The relationship between J_{SC} and incident light intensity (P_{light}) was fitted using the power-law equation

Table 1. Device performance parameters of PM6:L8-BO:$PC_{71}BM$-based inverted OSCs employing various CILs and 2PACz/MoO_x as the HTL with an active area of 0.14 cm^2

CILs	V_{oc} (V)	J_{sc} (mA/cm^2)	J_{sc} (calculated from IPCE, mA/cm^2)	FF (%)	PCE (%)
PDINN	0.84	24.48	23.23	71	14.58[a] (14.35 ± 0.23)[b]
PDINN/BCP	0.85	24.70	23.63	72	15.05[a] (14.75 ± 0.23)[b]
PDINN/Cu-BCP	0.87	25.18	24.40	76	16.70[a] (16.44 ± 0.23)[b]

[a]Champion device performance; [b]Average device performance calculated from 15 devices. PDINN: Aliphatic amine-functionalized perylene-diimide; CILs: cathode interlayers; BCP: bathocuproine; IPCE: incident-photon-to-current efficiency; PCE: power conversion efficiency; FF: fill factor.

$J_{SC} \propto (P_{light})^{\alpha}$, where α represents the exponential factor[45]. From Figure 3E, the α for the PDINN was 0.956, and this further increased to 0.980 and 0.981 for PDINN/BCP and PDINN/Cu-BCP, respectively. Therefore, devices employing the PDINN/Cu-BCP CIL exhibited more efficient charge extraction/collection and reduced bimolecular recombination compared with devices based on PDINN alone. Previous studies have attributed this deviation from unity to bimolecular recombination[46,47]. The light-intensity dependence of V_{OC} was further analyzed to identify the dominant recombination mechanism in the devices. In general, leakage pathways and trap-assisted recombination can increase the V_{OC}-light intensity slope beyond the ideal kT/q value. As shown in Figure 3F, the PDINN-based device, which exhibited a relatively high leakage current, showed a slope of 1.84 kT/q, indicating pronounced trap-assisted recombination. By contrast, the coordination-engineered PDINN/Cu-BCP device showed a smaller slope of 1.58 kT/q, suggesting that the Cu-BCP overlayer effectively suppresses trap-assisted recombination. To further evaluate the interfacial resistance, EIS was also performed at an applied bias close to the V_{OC} of each device, as shown in Figure 3G. Based on the fitted equivalent-circuit model, the extracted charge-transfer resistance (R_{CT}) decreased markedly from 70.49 Ω for PDINN to 29.85 Ω for PDINN/BCP and further to 15.75 Ω for PDINN/Cu-BCP [Supplementary Table 6]. The much lower values of the BCP-containing bilayers indicate more efficient interfacial charge transfer and reduced recombination losses compared with PDINN alone. In particular, the lowest R_{CT} observed for the PDINN/Cu-BCP device suggests that Cu coordination helps preserve a less resistive, more conductive cathode contact, consistent with its higher FF and overall superior device performance. As shown in Figure 3H, TRPL measurements were conducted to investigate how the different CILs affect the exciton decay dynamics of the photoactive layer. The progressive increase in the average photoluminescence (PL) decay lifetime from 2.959 ns for PDINN to 2.975 ns for PDINN/BCP and 3.047 ns for PDINN/Cu-BCP suggests altered exciton dynamics at the cathode-side interface. Combined with the higher J_{SC} and FF observed for PDINN/Cu-BCP devices, this trend is consistent with reduced non-radiative interfacial recombination rather than impeded charge extraction, indicating that Cu-coordination helps establish a more selective and less lossy cathode contact. The space-charge-limited current (SCLC) method was used to determine the electron mobility from the dark J-V characteristics of the electron-only devices. The electron-only device architecture was ITO/CIL/PM6:L8-BO:$PC_{71}BM$/PFN-Br/Ag, where the CIL was PDINN, PDINN/BCP, or PDINN/Cu-BCP, as shown in Figure 3I. The electron mobility was extracted by fitting the J-V curves using the Mott-Gurney equation.

$$J = \frac{9\varepsilon_0\varepsilon_r\mu_e V^2}{8d^3} \quad (1)$$

where J is the current density, ε_0 is the vacuum permittivity, ε_r is the assumed relative dielectric constant of 3.5, d is the thickness of the active layer set at 120 nm, V is the applied bias voltage, and μ_e is the electron mobility. The effective device area of electron-only devices was 0.14 cm^2. The extracted μ_e values are listed in

Supplementary Table 7. A progressive enhancement in electron mobility was observed, increasing from 4.96×10^{-3} (PDINN) to 6.69×10^{-3} $cm^2 V^{-1} s^{-1}$ (PDINN/BCP) and reaching 7.34×10^{-3} $cm^2 V^{-1} s^{-1}$ for the PDINN/Cu-BCP-based device. This increasing trend indicates that the Cu-BCP overlayer facilitates more efficient electron transport at the cathode-side interface, consistent with the enhanced conductivity, reduced charge-transfer resistance, and improved FF observed in the optimized device.

This study aims to improve the long-term durability of OSCs by improving the stability of the cathode-side interface. Accordingly, the operational durability of devices based on PDINN, PDINN/BCP, and PDINN/Cu-BCP was evaluated under three different aging conditions, as summarized in Figure 4. The air-storage test [Figure 4A] was conducted at RT with unencapsulated devices, whereas the thermal-humidity (65 °C/65% RH, Figure 4B) and photostability (1 sun, 25 °C/25% RH, Figure 4C) tests were performed on encapsulated devices. Among all configurations, the PDINN/Cu-BCP device consistently exhibited the slowest decay in normalized PCE, demonstrating the most robust cathode-side stability. The evolution of the individual photovoltaic parameters, including V_{OC}, J_{SC}, and FF, is further shown in Supplementary Figures 12-14. As summarized in Table 2, the T_{80} lifetime follows a consistent trend of PDINN < PDINN/BCP < PDINN/Cu-BCP under all three aging conditions. These results quantitatively confirm that the BCP-containing bilayers significantly prolong operational lifetime relative to PDINN alone, while the coordination-engineered PDINN/Cu-BCP device consistently exhibits the longest lifetime across all tested stress conditions. The superior stability of the PDINN/Cu-BCP device can be rationalized based on the following interfacial analyses. First, the Cu-BCP overlayer on top of PDINN improves the chemical robustness of the cathode-side interlayer, thereby helping to suppress interfacial degradation under stress. To further examine this effect, XPS measurements were performed on photo-aged CIL films, including ITO/PDINN, ITO/PDINN/BCP, and ITO/PDINN/Cu-BCP, as a representative aging analysis under illumination stress. Photo-aging was selected because the photostability data show a clear difference among the CILs at an early aging stage. After 100 h of continuous illumination, the PDINN- and PDINN/BCP-based devices already decrease to 72% and 78% of their initial PCE, whereas the PDINN/Cu-BCP-based device still maintains 97% of its initial performance. As shown in Supplementary Figure 15, after photo-aging, PDINN/Cu-BCP maintained the highest N 1s binding energy of 398.81 eV compared with PDINN (398.49 eV) and PDINN/BCP (398.56 eV). This indicates that the coordination-modified N environment is partially retained under illumination stress. Together with the Cu 2p signal, these results support the improved chemical robustness of the Cu-BCP-modified CIL, consistent with the enhanced photostability of the PDINN/Cu-BCP-based devices. Second, the more compact and uniform cathode-side morphology helps suppress leakage-current pathways and preserve contact selectivity during prolonged aging. This interpretation is supported by the aged-film AFM results shown in Supplementary Figures 16 and 17. After 200 h of thermal-humidity aging at 65 °C/65% RH, the PDINN/Cu-BCP/BHJ film exhibited the lowest roughness of R_q = 1.627 nm, compared with 1.747 nm for PDINN/BHJ and 1.651 nm for PDINN/BCP/BHJ. A similar trend was observed after 200 h of continuous 1-sun illumination, with the PDINN/Cu-BCP/BHJ film maintaining the lowest roughness (R_q = 1.661 nm), compared with 1.745 nm for PDINN/BHJ and 1.780 nm for PDINN/BCP/BHJ. These results indicate that the Cu-coordinated overlayer most effectively preserves the cathode-side interfacial morphology under both thermal-humidity and photo-aging conditions. Third, the aged-device EIS results further support the improved interfacial durability of bilateral bilayer interface engineering of OSC devices. As shown in Supplementary Figure 18 and Supplementary Table 8, the R_{CT} values of PDINN/Cu-BCP were substantially lower than those of the PDINN control after prolonged aging, indicating that the Cu-coordinated overlayer helps preserve stable interfacial charge-transfer characteristics during aging. After 1,000 h at 65 °C/65% RH, R_{CT} was 114.60 Ω for PDINN, 80.47 Ω for PDINN/BCP, and 29.30 Ω for PDINN/Cu-BCP. After 1,000 h of continuous 1-sun illumination, the corresponding R_{CT} values were 95.84, 39.68, and 34.07 Ω, respectively. These results show that the BCP-containing bilayers preserve interfacial charge-transfer characteristics much more effectively than PDINN alone after prolonged stress, while PDINN/Cu-BCP consistently exhibited the lowest aged R_{CT}. This behavior is primarily attributed to the chemically stabilized Cu-coordinated BCP overlayer, in which Cu-N

coordination modifies the electronic environment of the phenanthroline nitrogen atoms and provides additional chemical stabilization beyond conventional BCP. In addition, a more stable and compact interfacial structure may help suppress interfacial chemical reactions with NFAs and reduce the buildup of transport barriers under stress, particularly under thermal-humidity conditions[39,48].

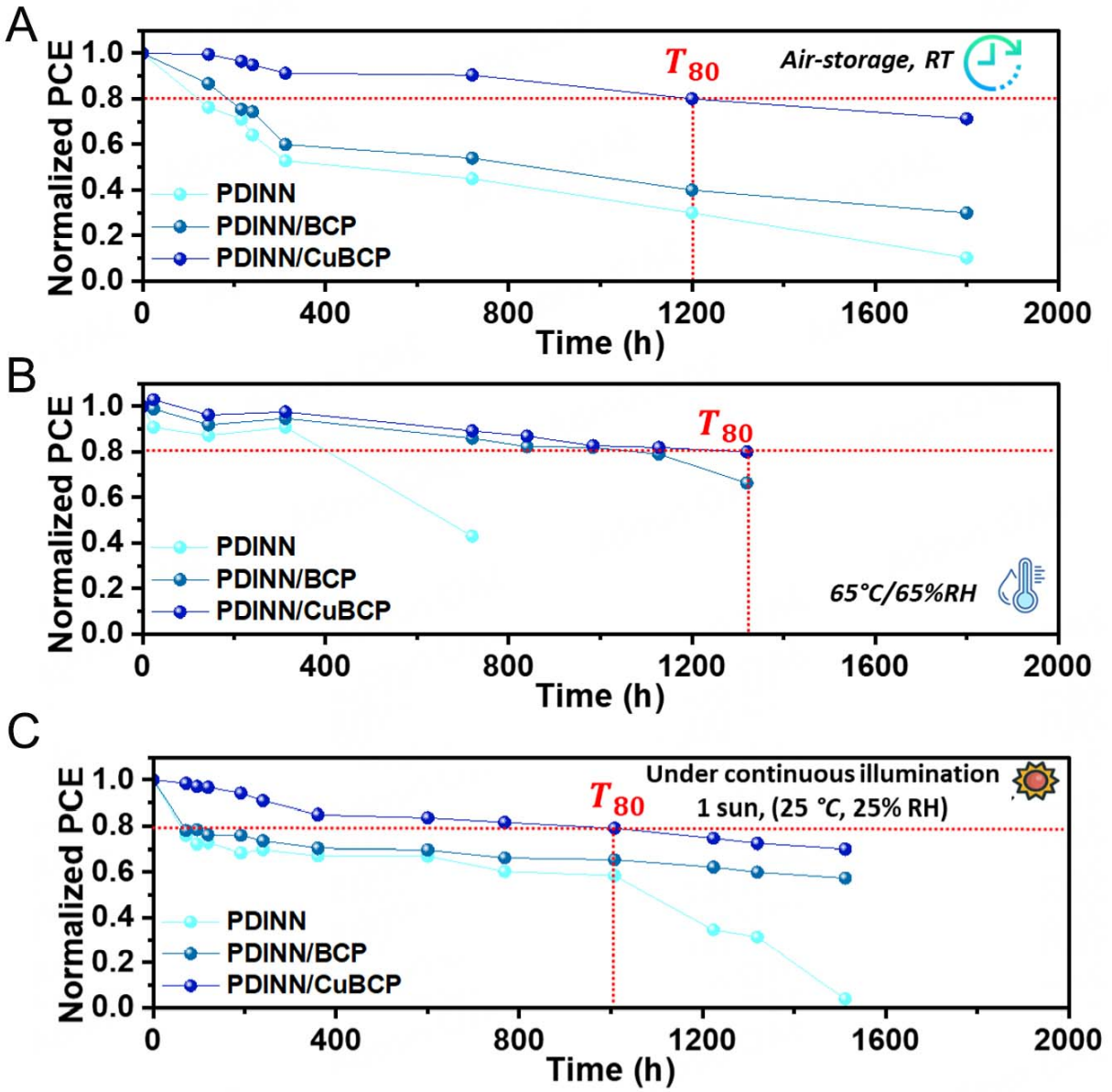

Figure 4. Stability characteristics of inverted OSCs employing different CILs. (A) Normalized PCE retention of devices with PDINN, PDINN/BCP, and PDINN/Cu-BCP during air storage at RT; (B) normalized PCE retention under thermal-humidity aging at 65 °C/65% RH. (C) normalized PCE retention under continuous 1 sun illumination at 25 °C and 25% RH.

Table 2. T_{80} lifetime comparison of OSC devices based on different CIL under various stress conditions

Stress condition	PDINN	PDINN/BCP	PDINN/Cu-BCP
Air storage, RT	144 h	216 h	1,200 h
Thermal-humidity, 65 °C/65% RH	400 h	1,080 h	1,320 h
Continuous 1-sun, 25 °C/25% RH	60 h	72 h	1,008 h

PDINN: Aliphatic amine-functionalized perylene-diimide; BCP: bathocuproine; RT: room temperature; OSC: organic solar cell; RH: relative humidity.

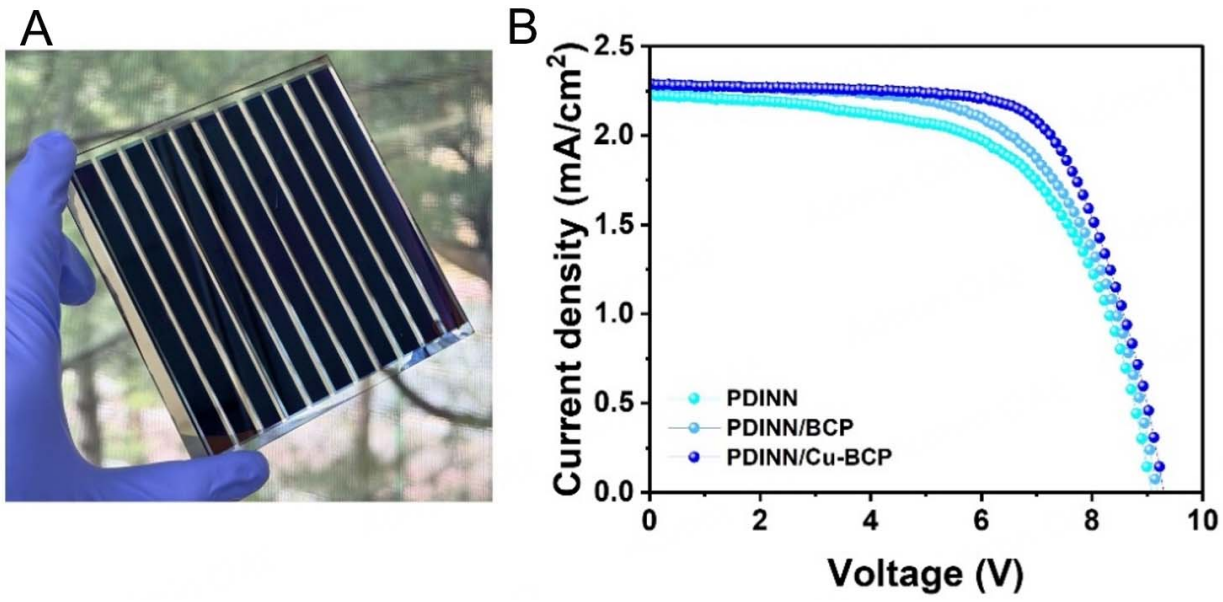

Figure 5. (A) Representative photograph of the fabricated module device (photographed by the authors); (B) J-V curves of the large-area module device with various CILs.

Table 3. Performance parameters of 54-cm² PM6:L8-BO:$PC_{71}BM$-based OSC modules employing different CILs

CILs	V_{oc} (V)	J_{sc} (mA/cm²)	FF (%)	PCE (%)
PDINN	9.07	2.23	61	12.33
PDINN/BCP	9.18	2.28	63	13.16
PDINN/Cu-BCP	9.30	2.30	68	14.57

PDINN: Aliphatic amine-functionalized perylene-diimide; PCE: power conversion efficiency; FF: fill factor; OSC: organic solar cell; CILs: cathode interlayers.

To verify the practical capability of the coordination-engineered PDINN/Cu-BCP, large-area OSC modules were fabricated on a 10 × 10 cm² glass/ITO substrate with an active area of 54 cm². A photograph of the fabricated module devices is presented in Figure 5A. As shown in Figure 5B and summarized in Table 3, the module performance strongly depends on the CIL configuration. The PDINN-based module exhibited a PCE of 12.33%, which increased to 13.16% after introducing the BCP overlayer. The highest module PCE of 14.57% was achieved with PDINN/Cu-BCP, corresponding to a CTM ratio of 87%. These results demonstrate the scalability of the Cu-BCP-modified cathode interface for large-area OSC modules.

CONCLUSIONS

We demonstrated a bilateral bilayer interfacial engineering approach that simultaneously enhances the photovoltaic performance and operational durability of inverted OSCs. An ultrathin Cu-coordinated BCP overlayer was incorporated onto PDINN, forming a chemically stabilized, electron-selective contact within the CIL region. Unlike conventional BCP, Cu-BCP provides additional stabilization through Cu-N coordination, which modifies the nitrogen electronic environment of BCP and improves the chemical robustness of the cathode-side interface while maintaining efficient electron extraction. When combined with the 2PACz/MoO_x anode bilayer, the resulting bilateral bilayer interface enables high-performance inverted OSCs. With this interfacial design, the optimized device delivered a high PCE of 16.70%, outperforming the PDINN (14.58%) and PDINN/BCP (15.05%) controls. More importantly, the optimized device consistently exhibited enhanced stability under multiple independent stress conditions, retaining

about 80% of its initial efficiency after 1,200 h in air storage, 1,320 h at 65 °C/65% RH, and 1,008 h under continuous 1-sun illumination, corresponding to the longest T_{80} lifetime among all tested devices. Furthermore, this interfacial strategy is compatible with large-area fabrication, delivering a module efficiency of 14.57% over a 54 cm^2 active area with an 87% CTM ratio. Therefore, these findings demonstrate that interfacial layers in high-performance OSCs must be designed not only for optimal energy-level alignment and charge selectivity, but also for enhanced stability under operational stress. The coordination-engineered interfacial strategy presented in this paper offers a viable pathway toward improving the durability and scalability of organic photovoltaic technologies.

DECLARATIONS

Authors' contributions

Conceptualization and design of the study: Wardani, N. K.
Data curation, visualization, resources, formal analysis, writing - original draft: Wardani, N. K.; Jahandar, M.
Funding acquisition, project administration: Kim, S.; Lim, D. C.
Supervision: Kim, Y. H.; Kim, S.; Lim, D. C.
Writing - review and editing: Wardani, N. K.; Jahandar, M.; Kim, Y. H.; Kim, S.; Lim, D. C.

Availability of data and materials

The data supporting our findings can be found in Supplementary Materials.

AI and AI-assisted tools statement

Not applicable.

Financial support and sponsorship

This research was supported by the National Research Council of Science & Technology (NST) grant by the Korean government (PNKA910) and the Fundamental Research Program of the National Research Foundation of Korea (RS-2024-00429694).

Conflicts of interest

All authors declared that there are no conflicts of interest.

Ethical approval and consent to participate

Not applicable.

Consent for publication

Not applicable.

Supplementary Materials

Supplementary Materials

REFERENCES

1. Yadagiri, B.; Narayanaswamy, K.; Sharma, G. D.; Singh, S. P. Carbazole core derived dyes: new non-fullerene acceptor for all small-molecule organic solar cells with very high open-circuit voltage of 1.12 V. *Dyes. Pigm.* **2021**, *194*, 109606. DOI
2. Xiao, X.; Chalh, M.; Loh, Z. R.; et al. Strategies to achieve efficiencies of over 19% for organic solar cells. *Cell. Rep. Phys. Sci.* **2025**, *6*, 102390. DOI
3. Li, M.; He, F. Organic solar cells developments: what's next? *Next. Energy.* **2024**, *2*, 100085. DOI
4. Liu, B.; Sandberg, O. J.; Qin, J.; et al. Inverted organic solar cells with an in situ-derived SiO_xN_y passivation layer and power conversion efficiency exceeding 18%. *Nat. Photonics.* **2025**, *19*, 195-203. DOI
5. Chen, C.; Wang, L.; Xia, W.; et al. Molecular interaction induced dual fibrils towards organic solar cells with certified efficiency over 20%. *Nat. Commun.* **2024**, *15*, 6865. DOI PubMed PMC

6. Shahid, A. M.; Rong, H. C.; Zhang, H.; et al. Manipulating heavy halogenated asymmetric terminals affords regio-regular hetero-fluorinated/brominated dual asymmetric acceptor with a binary photovoltaic efficiency of 20.3%. *Angew. Chem. Int. Ed.* **2026**, *65*, e3817518. DOI
7. Kadam, K. D.; Kim, H.; Khan, M. F.; et al. Role of interface engineering in amorphous InGaZnO ETL for non-fullerene organic solar cells. *Surf. Interfaces.* **2024**, *44*, 103626. DOI
8. Jin, W.; Ginting, R. T.; Jin, S.; Kang, J. Highly stable and efficient inverted organic solar cells based on low-temperature solution-processed PEIE and ZnO bilayers. *J. Mater. Chem. A.* **2016**, *4*, 3784-91. DOI
9. Xu, X.; Li, D.; Yuan, J.; Zhou, Y.; Zou, Y. Recent advances in stability of organic solar cells. *EnergyChem* **2021**, *3*, 100046. DOI
10. Lee, S.; Jin, J. S.; Moon, H.; et al. Long-term thermal stability of nonfullerene organic solar cells via facile self-assembled interface passivation. *ACS. Energy. Lett.* **2023**, *8*, 3989-98. DOI
11. Liang, H.; Bi, X.; Chen, H.; et al. A rare case of brominated small molecule acceptors for high-efficiency organic solar cells. *Nat. Commun.* **2023**, *14*, 4707. DOI PubMed PMC
12. Xu, X.; Xiao, J.; Zhang, G.; et al. Interface-enhanced organic solar cells with extrapolated T80 lifetimes of over 20 years. *Sci. Bull.* **2020**, *65*, 208-16. DOI
13. Liu, B.; Qin, J.; Luo, Q.; Ma, C. Multifunctional interface engineering enables efficient and stable inverted organic photovoltaics. *Nat. Commun.* **2025**, *16*, 4880. DOI PubMed PMC
14. Günther, M.; Lotfi, S.; Rivas, S. S.; et al. The neglected influence of zinc oxide light-soaking on stability measurements of inverted organic solar cells. *Adv. Funct. Mater.* **2023**, *33*, 2209768. DOI
15. Günther, M.; Blätte, D.; Oechsle, A. L.; et al. Increasing photostability of inverted nonfullerene organic solar cells by using fullerene derivative additives. *ACS. Appl. Mater. Interfaces.* **2021**, *13*, 19072-84. DOI
16. Yu, Y.; Wang, J.; Cui, Y.; et al. Cost-effective cathode interlayer material for scalable organic photovoltaic cells. *J. Am. Chem. Soc.* **2024**, *146*, 8697-705. DOI
17. Nie, H.; Huang, S.; Lai, C.; et al. Water/Alcohol-soluble conjugated polymers based on cyclopentadithiophene and fluorene as cathode interlayers elevate the stability and efficiency in organic solar cells. *ACS. Appl. Energy. Mater.* **2022**, *5*, 9495-502. DOI
18. Kang, Q.; Ye, L.; Xu, B.; et al. A printable organic cathode interlayer enables over 13% efficiency for 1-cm^2 organic solar cells. *Joule* **2019**, *3*, 227-39. DOI
19. Wang, Y.; Zhou, D.; Lan, S.; et al. Small molecule perylene diimide derivatives with different bay site modifications as cathode interface layers for organic solar cells. *Chem. Eng. J.* **2024**, *496*, 154206. DOI
20. Shan, C.; Liu, T.; Zhou, J.; et al. High-performance organic solar cell and self-power photodetector with chemically robust, near-infrared acceptor enabled by strengthening interfacial contact and compositional modulation. *Chem. Eng. J.* **2023**, *471*, 144451. DOI
21. Yao, J.; Qiu, B.; Zhang, Z.; et al. Cathode engineering with perylene-diimide interlayer enabling over 17% efficiency single-junction organic solar cells. *Nat. Commun.* **2020**, *11*, 2726. DOI PubMed PMC
22. Liu, T.; Sun, L.; Xie, C.; Wang, W.; Qin, F.; Zhou, Y. Bathocuproine as a cathode interlayer for nonfullerene organic solar cells with efficiency over 17%. *J. Mater. Chem. A.* **2021**, *9*, 23269-75. DOI
23. Yoshida, H. Electron transport in bathocuproine interlayer in organic semiconductor devices. *J. Phys. Chem. C.* **2015**, *119*, 24459-64. DOI
24. Wang, X.; Liang, Q.; Zhang, A.; et al. Amide-based cathode interfacial layer with dual-modification mechanisms enables stable organic solar cells with high efficiency achieving 20%. *J. Am. Chem. Soc.* **2025**, *147*, 9261-72. DOI
25. Alishan, Y.; Joseph, A.; Pillai, A. B.; et al. Metal nanoclusters for interface engineering and improved photovoltaic performance in organic solar cells. *ACS. Nano.* **2024**, *18*, 35383-92. DOI
26. Jahandar, M.; Prasetio, A.; Lee, C.; et al. Highly efficient flexible organic photovoltaic modules for sustainable energy harvesting under low-light condition via suppressing voltage-drop by metal-mediated cross-linkable polymer interfacial layer. *Chem. Eng. J.* **2022**, *448*, 137555. DOI
27. Fukagawa, H.; Suzuki, K.; Ito, H.; et al. Understanding coordination reaction for producing stable electrode with various low work functions. *Nat. Commun.* **2020**, *11*, 3700. DOI PubMed PMC
28. Hao, X.; Wang, S.; Fu, W.; Sakurai, T.; Masuda, S.; Akimoto, K. Novel cathode buffer layer of Ag-doped bathocuproine for small molecule organic solar cell with inverted structure. *Org. Electron.* **2014**, *15*, 1773-9. DOI
29. Sathyadevan, Nair. A. C.; Rajan, A.; Raj, K. P. A.; et al. Fine tuning the work function of ZnO cathode buffer layers in organic solar cells by phenanthroline coordination. *ACS. Appl. Energy. Mater.* **2024**, *7*, 9011-22. DOI
30. Jing, J.; Dong, S.; Zhang, K.; et al. In-situ self-organized anode interlayer enables organic solar cells with simultaneously simplified processing and greatly improved efficiency to 17.8%. *Nano. Energy.* **2022**, *93*, 106814. DOI
31. Jeong, S.; Rana, A.; Kim, J. H.; et al. New ternary blend strategy based on a vertically self-assembled passivation layer enabling efficient and photostable inverted organic solar cells. *Adv. Sci.* **2023**, *10*, 2206802. DOI PubMed PMC

32. Bin, Z.; Dong, G.; Wei, P.; et al. Making silver a stronger n-dopant than cesium via in situ coordination reaction for organic electronics. *Nat. Commun.* **2019**, *10*, 866. DOI PubMed PMC
33. Huang, Q.; Jing, J.; Zhang, K.; et al. Simultaneous improvement of efficiency and stability of inverted organic solar cell*via* composite hole transport layer. *J. Mater. Chem. A.* **2022**, *10*, 23973-81. DOI
34. Lin, Y.; Zhang, Y.; Magomedov, A.; et al. 18.73% efficient and stable inverted organic photovoltaics featuring a hybrid hole-extraction layer. *Mater. Horiz.* **2023**, *10*, 1292-300. DOI
35. Chambon, S.; Derue, L.; Lahaye, M.; Pavageau, B.; Hirsch, L.; Wantz, G. MoO_3 thickness, thermal annealing and solvent annealing effects on inverted and direct polymer photovoltaic solar cells. *Materials* **2012**, *5*, 2521-36. DOI PMC
36. Zhou, D.; Quan, J.; Zhang, H.; et al. Small-molecule electron transport layer with siloxane-functionalized side chains for nonfullerene organic solar cells. *ACS. Appl. Mater. Interfaces.* **2022**, *14*, 54063-72. DOI
37. Xu, X.; Peng, Q. Hole/Electron transporting materials for nonfullerene organic solar cells. *Chem. A. Eur. J.* **2022**, *28*, e202104453. DOI
38. Hu, L.; Liu, Y.; Mao, L.; et al. Chemical reaction between an ITIC electron acceptor and an amine-containing interfacial layer in non-fullerene solar cells. *J. Mater. Chem. A.* **2018**, *6*, 2273-8. DOI
39. Lai; X; Chen; S; Gu; X; et al. Phenanthroline-carbolong interface suppress chemical interactions with active layer enabling long-time stable organic solar cells. *Nat. Commun.* **2023**, *14*, 3571. DOI PubMed PMC
40. Jiang, P.; Hu, L.; Sun, L.; Li, Z.; Han, H.; Zhou, Y. On the interface reactions and stability of nonfullerene organic solar cells. *Chem. Sci.* **2022**, *13*, 4714-39. DOI PubMed PMC
41. Lai, T.; Tsang, S.; Manders, J. R.; Chen, S.; So, F. Properties of interlayer for organic photovoltaics. *Mater. Today.* **2013**, *16*, 424-32. DOI
42. Walker, B.; Choi, H.; Kim, J. Y. Interfacial engineering for highly efficient organic solar cells. *Curr. Appl. Phys.* **2017**, *17*, 370-91. DOI
43. Alharbi, N. S.; Wang, C.; Alsaadi, F. E.; Rabah, S. O.; Tan, Z. A general approach of adjusting the surface-free energy of the interfacial layer for high-performance organic solar cells. *Adv. Sustain. Syst.* **2020**, *4*, 2000054. DOI
44. Yin, Z.; Wei, J.; Zheng, Q. Interfacial materials for organic solar cells: recent advances and perspectives. *Adv. Sci.* **2016**, *3*, 1500362. DOI PubMed PMC
45. Schilinsky, P.; Waldauf, C.; Brabec, C. J. Recombination and loss analysis in polythiophene based bulk heterojunction photodetectors. *Appl. Phys. Lett.* **2002**, *81*, 3885-7. DOI
46. Hartnagel, P.; Kirchartz, T. Understanding the light-intensity dependence of the short-circuit current of organic solar cells. *Advcd. Theory. Sims.* **2020**, *3*, 2000116. DOI
47. Zeiske, S.; Li, W.; Meredith, P.; Armin, A.; Sandberg, O. J. Light intensity dependence of the photocurrent in organic photovoltaic devices. *Cell. Rep. Phys. Sci.* **2022**, *3*, 101096. DOI
48. Li, Z.; Ho, Chiu. K.; Shahid, Ashraf. R.; et al. Toward improved lifetimes of organic solar cells under thermal stress: substrate-dependent morphological stability of PCDTBT:PCBM films and devices. *Sci. Rep.* **2015**, *5*, 15149. DOI PubMed PMC